Computational Fluid Dynamics Simulation of Chemical Vapor Synthesis of WC Nanopowder from Tungsten Hexachloride

Taegong Ryu[1], Miguel Olivas-Martinez[1], Hong Yong Sohn[1*], Z. Z. Fang[1], and Terry A. Ring[2]

[1]Department of Metallurgical Engineering
[2]Department of Chemical Engineering
University of Utah, Salt Lake City, Utah 84112, USA

Abstract

The chemical vapor synthesis (CVS) reactor for the preparation of WC nanopowder from tungsten hexachloride was simulated by a two-dimensional multiphase computational fluid dynamics (CFD) model. The model solves the gas-phase governing equations of overall continuity, momentum, energy, and species mass transport inside a tubular reactor system. The population balance model is coupled with the gas-phase equations to describe the formation and growth of WC nanoparticles. The model has been validated with experimental data in terms of average particle size and concentration of unreacted precursor at the outlet. The contours of temperature, velocity, species concentration and particle size distribution (PSD) inside the tubular reactor were computed.

* Corresponding author. Tel.: +1-801-581-5491; fax: +1-801-581-4937

Email address: h.y.sohn@utah.edu

1. Introduction

Due to the much desired properties of high hardness and good wear resistance, tungsten carbide (WC) is widely used as a hard material in many industrial applications such as metalworking, drilling and mining industries under high pressure, high temperature, and corrosive environments. Its mechanical properties such as hardness, compressive strength, and transverse rupture depend on the composition and microstructural parameters such as the grain size of WC [1-4]. Previous investigations [5-11] have shown that the reduction of tungsten carbide grain size provides a significant improvement in the mechanical properties. The reduction in size of the structure also means an increase in the dislocation density and the amount of grain boundaries per unit area. Furthermore, nanosized powder changes the response during sintering, which results in lower sintering temperatures and shorter times to attain dense but small grain size structures. Therefore, the production of nanosized tungsten carbide powder is critical.

Nanosized tungsten carbide powders have been produced by various methods such as thermo-chemical spray drying process [12,13], mechanical alloying (MA) [14-16], and chemical vapor condensation (CVC) [17]. Chemical vapor synthesis (CVS) is a process for making fine solid particles by the vapor-phase chemical reactions of precursors. The chemical vapor synthesis (CVS) process, which has been applied to the synthesis of metallic and intermetallic powders at the University of Utah, has several advantages in producing nanograined powders having compositional uniformity, high purity, and small grain sizes [18-20].

The CVS process of WC is carried out by the reduction of vapor-phase reactant precursors and subsequent carburization by gaseous carburization agents such as hydrocarbon [21]. Tungsten metal compounds such as tungsten hexachloride (WCl_6) [22], tungsten hexafluoride (WF_6) [23], and tungsten hexacarbonyl ($W(CO)_6$) [24] are generally favored as the precursor because of their relatively low volatilization temperatures as well as the ease of reduction by hydrogen. Several carburizing agents have also been used such as propane (C_3H_8), acetylene (C_2H_2), and methane (CH_4). Methane is the most commonly used carburizing agent because it is easy to control the amount of carbon reacted and stable up to a high temperature [25].

Although considerable work to produce nanosized WC powder by gas-phase reactions has been conducted, the mechanism of WC particle formation is not well understood. This process is very complicated with mass and heat transfer, chemical reactions, and particle formation all occurring simultaneously.

In this work, a commercial CFD code, FLUENT 6.3.26 [26,27], was used to simulate the chemical vapor synthesis of WC in a tubular reactor. WCl_6 was used as the precursor with reactant gases H_2 and CH_4 as the reducing and carburizing agents, respectively. The CVS process was simulated to obtain the velocity profile, temperature profile, species concentration distribution, and particle size distribution (PSD). This work was aimed at developing a CFD model for the WC preparation by chemical vapor synthesis and validating it with experimental results obtained in a tubular reactor.

2. Model Formulation

2.1 Governing Equations

The model formulation involves the description of the fluid flow, heat and mass transfer processes, chemical reactions, and particle formation and growth. The population balance model (PBM) was used to describe the particle formation and growth as well as the particle size distribution in the tubular reactor system. The following assumptions were made: (a) steady state, (b) axisymmetrical 2D laminar flow, and (c) spherical particles. The partial differential equations shown below were solved to compute velocity, temperature, and species concentration distributions inside the tubular reactor.

Continuity equation:

$$\nabla \cdot (\rho \vec{v}) = 0 \tag{1}$$

where ρ is the density of the mixture and $\vec{v}$ is the velocity vector.

Momentum conservation equations:

$$\nabla \cdot (\rho \vec{v}\vec{v}) = -\nabla p + \nabla \cdot (\bar{\bar{\tau}}) \tag{2}$$

$$\bar{\bar{\tau}} = \mu[(\nabla \cdot \vec{v}) - \frac{2}{3}\nabla \cdot \vec{v} I] \tag{3}$$

where p is the static pressure, $\bar{\bar{\tau}}$ is the stress tensor, μ is the molecular viscosity, I is the unit tensor, and the second term on the right-hand side of equation (3) represents the effect of volume dilation.

Energy equation:

$$\rho C_p(\vec{v}\cdot\nabla T) = k\nabla^2 T + \sum_{i=1}^{n} h_i M_i \cdot \omega_i \tag{4}$$

where C_p is the heat capacity at constant pressure, T is the temperature, k is the thermal conductivity, h_i is the enthalpy of species i, M_i is the molecular weight of species i, and ω_i is the net production rate per volume of species i by chemical reaction.

Species transport equation:

$$\nabla\cdot(\rho\vec{v}Y_i) = -\nabla\cdot\vec{J}_i + R_i + S_i \tag{5}$$

where R_i is the net rate per volume of production of species i by chemical reaction and S_i is the rate per volume of addition to the gas phase from the dispersed phase plus any user-defined sources, Y_i is the mass fraction of species i, and J_i is the diffusion flux of species i, which arises due to concentration gradients. Total six species considered in this simulation were WCl_6, CH_4, H_2, Ar, WC, and HCl based on the chemical reaction as follows:

$$WCl_6(g) + CH_4(g) + H_2(g) = WC(s) + 6HCl(g) \tag{6}$$

The changes in the number density of WC particles in the size range between L and $L+dL$ in the tubular reactor is represented by the population balance model (PBM) given by the following equation:

$$\frac{\partial}{\partial L}(nG) + \nabla\cdot(n\vec{v}) = Birth - Death \tag{7}$$

where n is the particle number density function, L is the particle size (particle diameter), and G is the growth rate of particles. The birth and death source terms represent the rates of particles birth and death due to brakeage, aggregation, and other related phenomena. The boundary condition [26,27] at $L=0$ for the integration of the first term of Eq. (7) is obtained from

$$n\cdot dL\big|_{L=0} = J\cdot dt = J\left(\frac{dL}{G}\right) \tag{8}$$

and thus

$$n|_{L=0} = \frac{J}{G} \tag{9}$$

where J represents the rate of nucleation of particles.

The size-distribution characteristics of the WC particles were expressed in terms of the appropriate moments of the size distribution as follows:

$$m_i = \int_0^\infty L^i n(L) dL \tag{10}$$

The population balance model, Equation (7), was solved by means of the quadrature method of moments (QMOM), considering the first six moments of the particle number density function.

2.2. Particle formation and growth

The mechanisms of nucleation and growth of WC nanoparticles from the simultaneous reduction and carburization of WCl_6 are not well understood. Based on the Kelvin equation [28] which predicts the critical nucleus size, several researchers agree that the nucleation of particles of high boiling point like WC nanoparticles is a collision-controlled process. Once the WC monomers are formed by chemical reactions, the monomers are considered as thermodynamically stable particles since the critical nucleus size is much smaller than the monomer size. Thus, it is said that the nucleation is indistinguishable from chemical reaction [28,29]. Here, the nucleation rate of WC is given by a first-order reaction rate law, which is dependent on the concentrations of WCl_6 and CH_4. The nucleation rate was thus expressed by

$$J = k_n N_A C_{WCl_6} C_{CH_4} \tag{11}$$

where, J is the nucleation rate ($\#\cdot s^{-1}\cdot m^{-3}$), k_n is the nucleation rate constant ($m^3\cdot kmol^{-1}\cdot s^{-1}$), N_A is the Avogadro constant ($molecules\cdot kmol^{-1}$), and C_{WCl_6} and C_{CH_4} are the molar concentration ($kmol\cdot m^{-3}$) of WCl_6 and CH_4, respectively.

The growth of WC nanoparticles takes place due to the surface chemical reaction of WCl_6 and CH_4 at the particle surface and the mass transfer of precursors to the particle

surface. The growth rate under the control of chemical reaction kinetics [28,29] is expressed by

$$G_c = k_g C_{WCl_6} C_{CH_4} \tag{12}$$

where k_g represents the growth rate constant ($m^7 \cdot kmol^{-2}\ s^{-1} \cdot$), C_{WCl_6} and C_{CH_4} are the molar concentration ($kmol \cdot m^{-3}$) of WCl_6 and CH_4, respectively. The linear growth rate of a particle under the mass transfer control, assumed to be controlled by the diffusion of the largest molecule in the system (WCl_6), is given by

$$G_m = 4 V_{mol} D_{WCl_6} \frac{m_0}{m_1} C_{WCl_6} \tag{13}$$

where V_{mol} is the molar volume of the WC particle ($m^3 \cdot mol^{-1}$), D_{WCl_6} ($m^2 \cdot s^{-1}$) is the diffusion coefficient of WCl_6 in the mixture, which is a function of temperature, m_0 is the zeroth moment ($1 \cdot m^{-3}$) of the particle size distribution (PSD), m_1 is the first moment (m/m^3) (thus, m_1/m_0 represents the number-averaged particle size), and C_{WCl_6} is the molar concentration ($kmol \cdot m^{-3}$) of WCl_6.

The overall growth rate G under the combined control of surface chemical reaction and mass transfer can be expressed by

$$G = \frac{G_c G_m}{G_c + G_m} \tag{14}$$

In this system studied, the growth rate under the control of surface chemical reaction was the limiting factor, which means that the growth rate under the control of mass transfer is much faster than the growth rate by the surface chemical reaction. This is because gas-solid mass transfer is extremely fast for small particles [30].

In terms of the particle growth rate, the rate of increase of the solid mass per unit volume of the system in the overall mass balance is given by

$$Source = (\pi / 2) m_2 G \rho_{WC} \tag{15}$$

where ρ_{WC} is the solid density ($kg \cdot m^{-3}$) and m_2 is the second moment of the PSD (m^2/m^3), which represents the total surface area of particles per unit volume of the reactor.

2.3. Boundary conditions

Figure 1 shows the experimental wall temperature profile and the simulated reactor geometry. The inner diameter and total length of reactor simulated were 5.4 cm and 38 cm, respectively. The temperature at the inlet was 835°C and after 3.5 cm and 12 cm in distance from the inlet it was increased to 1000°C and 1400°C, respectively. According to Hojo et al. [31] and our experimental work [21], substantial WC formation from WCl_6 starts to occur above 1000°C.

Our initial 3-D simulation runs considering the entire reactor geometry for reaction temperatures of 1200, 1300 and 1400°C showed that all species were mixed homogeneously before the reactant gases approached a temperature of 600, 720, 835°C, respectively. These values were then adopted as the inlet temperatures. The experimental temperature profile shown in Figure 1 was used as the boundary condition at the reactor wall. The mass fractions of WCl_6, CH_4, and H_2 at the inlet were 0.0347, 0.0483, and 0.0152, respectively, based on the experimental conditions [21]. At the wall, zero-gradient (zero-flux) boundary conditions were applied for all species (standard wall function). The 3-D simulations also showed that the flow of the mixture became symmetric around the reactor centerline before the flow of the mixture reached the reaction zone. This evidence allowed us to do the simulation in a 2-D axisymmetrical framework.

3. Results and discussion

3.1. Determination of nucleation rate and growth rate constants

The nucleation rate and growth rate are important factors that determine the particle size distribution (PSD). However, it is extremely difficult to determine the nucleation rate constant (k_n) and growth rate constant (k_g) by experimental measurements for the synthesis of WC nanoparticles. Because there were no measured data on these parameters, we first obtained these parameters by adjusting k_n and k_g and comparing the computed results with experimental measurements of average particle size and the coefficient of variation in some cases. In the experimental results, in which WC was synthesized under the conditions of WCl_6 feeding rate of 0.04 g/min, H_2 flow rate of 0.25 L/min (25°C, 86.1 kPa), CH_4 flow rate of 0.1 L/min (25°C, 86.1 kPa), and Ar flow rate of 0.75 L/min (25°C, 86.1 kPa), and the reaction temperature of 1400°C, the average particle size based on

specific surface area measurement was 22.2 nm and the coefficient variation (C.V.) was 0.18.

The experimental average particle size (D) was calculated from the measured specific surface area (A) and particle density (ρ) by the following equation under the assumption of spherical shape:

$$D=\frac{6}{\rho A} \tag{16}$$

The coefficient of variation (C.V.) means the degree of spread of the size distribution. It is represented as the ratio of the standard deviation of a distribution (S) to its mean size (D), as expressed below:

$$C.V.=\frac{S}{D} \tag{17}$$

In the simulation results, the average particle size based on specific surface area was derived by the following method:

$$L_a=\frac{6}{\rho A}=\frac{6}{\rho\frac{s}{\rho V}}=\frac{6V}{s}=\frac{6\cdot\frac{\pi}{6}\int_0^\infty L^3 n(L)dL}{\pi\cdot\int_0^\infty L^2 n(L)dL}=\frac{m_3}{m_2} \tag{18}$$

where L_a is the calculated average particle size, S_a is the calculated surface area of the particles, V is the volume of the particles, m_2 is the second moment, m_3 is the third moment, and $n(L)$ is the number density function.

The coefficient of variation (C.V.) is given in terms of the moments as follow:

$$C.V.=\sqrt{\frac{m_4 m_2}{(m_3)^2}-1} \tag{19}$$

However, in the experimental results, the particle size measurement was from the rather limited number of particles. Thus, in view of this, average particle size and the concentration of WCl_6 at outlet were mainly considered to determine the values of k_n and k_g based on the experimental results that the reaction was complete at this temperature indicating no unreacted WCl_6. The obtained kinetic constants, k_n and k_g were 1×10^{-1} ($m^3\cdot kmol^{-1}\cdot s^{-1}$) and 7.5 ($m^7\cdot kmol^{-2}\ s^{-1}\cdot$), respectively, as shown in Table 1.

From Table 1, it is observed that the calculated average particle size increases as the growth rate constant increases at a constant nucleation rate. Thus, to find the best set of nucleation rate and growth rate constants, first the nucleation rate constant was fixed and the growth rate constant varied based on the experimental average particle size and the concentration of unreacted WCl_6 at the outlet. From the results, if the nucleation rate constant was smaller than 1×10^{-1} the concentration of unreacted WCl_6 increased even though the predicted average particle size matched the experimental value. In addition, if this value was higher than 1×10^{-1}, it resulted in an unstable numerical process, leading to a divergent solution.

3.2. Temperature, velocity, and concentration profile

From the initial computation, the nucleation rate constant and growth rate constant were fixed at 1×10^{-1} ($m^3\cdot kmol^{-1}\cdot s^{-1}$) and 7.5 ($m^7\cdot kmol^{-2}\ s^{-1}\cdot$), respectively, for further simulation work. Figure 2 shows the temperature contours with fixed nucleation and growth rate constants obtained numerically as mentioned above. The velocity magnitude of the mixture is shown in Figure 3, in which the total linear velocity of reactant gases at the inlet was 0.0298 m/s. The inlet and the plateau wall temperatures were 835°C and 1400°C, respectively. The highest velocity was observed at the center of reaction zone and the lowest velocity was observed near the wall of the reactor. These converged results are reasonable as far as the temperature and velocity profile are concerned.

The contours of mole fraction of WCl_6 in Figure 4 show that WCl_6 was consumed completely and that the reaction with hydrogen and methane occurred rapidly. Figures 5 and 6 show the contours of mole fractions of hydrogen and methane, respectively, in which they are seen to be consumed rapidly for WC formation. These results were reasonable considering that the reaction in the vapor phase occurs rapidly.

Figures 7 and 8 show the contours of nucleation rate and growth rate obtained by applying the kinetic constants as discussed previously. These results were in good agreement with the WC formation reaction, in which the nucleation and growth of WC particles start rapidly above 1000°C.

3.3. Particle size distribution

As mentioned earlier, the nucleation rate and growth rate constants are two important factors that determine the particle size distribution. Figure 9 shows the contours of simulated WC particle size in the tubular reactor, in which the nucleation rate constant and growth rate constant were fixed at 1×10^{-1} ($m^3\cdot kmol^{-1}\cdot s^{-1}$) and 7.5 ($m^7\cdot kmol^{-2}\cdot s^{-1}$), respectively.

From the results, it is observed that the largest particle size of 41 nm was near the reactor wall, where the linear velocity of mixture is lowest, and the average particle size at the outlet was 21 nm.

If more detailed experimental data on the average particle size are available, additional model verification and validation can be conducted. The nucleation rate and growth rate constants (k_n and k_g) obtained at 1400°C of reaction temperature were applied to verify these constants by the comparison of average particle size obtained at different CH_4/WCl_6 molar ratios in the reaction. From the simulation work, in which the nucleation rate and growth rate constants (k_n and k_g) were 1×10^{-1} ($m^3\cdot kmol^{-1}\cdot s^{-1}$) and 7.5 ($m^7\cdot kmol^{-2}\cdot s^{-1}$), respectively, the average particle size was 21 nm at CH_4/WCl_6 ratio of 35, 20 nm at CH_4/WCl_6 ratio of 17, 19 nm at CH_4/WCl_6 ratio of 8, and 17 nm at CH_4/WCl_6 ratio of 3. The simulation results showed that the average particle size slightly decreased with a decrease in methane concentration in the reaction but the change was not large. The experimentally determined particle size from a rather limited number of particles was not affected by methane concentration. Thus, the rather small variation (4 nm) in the simulation can be acceptable to be consistent with experimental results.

According to the experimental results, the average particle size decreased with a decrease in reaction temperature. To determine the best set of nucleation rate and growth rate constants at different reaction temperatures, the same approach of adjusting these values to obtain the average particle size close to the experimental results was applied. At each temperature, a set of constants was obtained to determine the temperature dependence of the nucleation and growth phenomena. The optimum values of nucleation rate and growth rate constants that matched the experimental data at 1300°C and 1200°C were 1×10^{-1} ($m^3\cdot kmol^{-1}\cdot s^{-1}$) and 6 ($m^7\cdot kmol^{-2}\cdot s^{-1}$), and 1×10^{-1} ($m^3\cdot kmol^{-1}\cdot s^{-1}$) and 3.3 ($m^7\cdot kmol^{-2}\cdot s^{-1}$), respectively.

The intrinsic chemical reaction is fast at higher reaction temperatures. From the simulation results, the nucleation rate constant was the same, which is consistent with a previous result for a system in which nucleation was mainly related to the degree of turbulence [32]. Note, however, that the temperature range tested was rather narrow. Therefore, turbulence mixing determines the nucleation rate in this study. On the other hand, the growth rate constant decreased with a decrease in the reaction temperature from 1400°C to 1200°C. This indicates that the particle size was mainly affected by the dependence of the growth rate on the reaction temperature.

The temperature dependence of the growth rate constant is expressed by the following Arrhenius equation:

$$k_g = A \cdot \exp(-E_a/RT) \tag{20}$$

where, A is the pre-exponential factor (consistent units), E_a is the apparent activation energy (J/mol), and R is the gas constant (J/mol·K). From the plot of ln k_g vs 1/T(K), the slope was -10202, which gives an apparent activation energy value of 84.2 (kJ/mol), as shown in Figure 10. This result must be considered approximate because experimental data were obtained only at three temperatures.

10202 × 1.98 = 20404 from Hole

3.4. Comparison between the Simulation Results of SiO_2 and WC Nanoparticles

The direct determination of the actual kinetics of nucleation and growth of nanoparticles synthesized in the gas phase is a very complicated task. It may include the measurement of the gas-phase concentration of products and precursors inside the reactor by means of in-situ spectroscopic techniques. Most of the previous modeling work on the gas-phase synthesis of nanoparticles involves one or several parameters fitted to yield agreements with the available experimental information such as average particle size, which is the most common and important parameter to be determined experimentally. In this laboratory, the simulation of the synthesis of SiO_2 nanoparticles in a flame reactor was also carried out. Simplified expression for the rate of nucleation and growth were proposed and two rate constants were adjusted as described in this article [30].

Although this fitting approach is empirical and the operating conditions (i.e. reaction temperature, residence time, etc.) of the synthesis processes of SiO_2 and WC nanoparticles are different, it is of interest to compare the predicted rates of nucleation

and growth of particles in both processes. As a result, an order of magnitude comparison between both rate processes was performed. Since the average particle size was the target variable that was adjusted by fitting the rate constants, the comparison between the predicted average particle sizes in both synthesis processes will be meaningful. The average particle sizes were 15.6 and 21.7 nm for SiO_2 and WC nanoparticles, respectively. It was found the magnitudes of the nucleation and growth rates of nanoparticles in both processes were in the order of 10^{18} # m^{-3} s^{-1} and 10^{-7} m s^{-1}, respectively. This result correlates well with the fact that both materials, SiO_2 and WC, show low vapor pressure at their reaction temperatures and, as a result, the nucleation rate is mainly affected by the degree of turbulence and the growth rate is controlled by surface reaction at the particle. This finding indicates that the proposed fitting approach is representing reasonable the actual phenomena taking place in both synthesis processes.

4. Conclusions

The chemical vapor synthesis (CVS) of WC nanopowder from tungsten hexachloride in a tubular reactor was simulated by a two-dimensional multiphase computational fluid dynamics (CFD) model. A parametric study was conducted to determine the nucleation and growth rate constants. Experimental results obtained for the synthesis of WC nanopowder from WCl_6 with H_2 and CH_4 in a tubular reactor system were used to validate the model. The combination of nucleation rate and growth rate constants that yielded the best agreement with experimental data was determined. The simulation would be improved further when more experimental results and more accurate nucleation and growth model are available. However, it should be noted that this work is the first application of CFD to the chemical vapor synthesis of WC nanopowder. The simulation results have been matched with the experimental data under the conditions tested. The model tested in this work will also predict experimental results for other sets of experimental conditions. This simulation tool shows a significant potential for the optimization and scaling up of the chemical vapor synthesis process.

Acknowledgments

This material is based upon work supported by the U.S. Department of Energy under Award No. DE-FC36-04GO14041 with cost sharing by Kennametal and Smith International and technical collaboration with Idaho National Laboratory. MOM expresses his gratitude to CONACyT (Consejo Nacional de Ciencia y Tecnología / National Council of Science and Technology) for the scholarship granted to pursue Ph.D. studies. The authors also wish to acknowledge Fluent. Inc., the provider of the FLUENT® software used in this project. Fluent Inc. is a wholly-owned subsidiary of ANSYS, Inc. See www.ansys.com for more information.

Reference

1. Upadhyaya, G.S., 2002. Cemented Tungsten Carbide, New York: Noyes Publications, pp. 1.

2. Petersson, A., Ågren, J., 2004. Constitutive behaviour of WC-Co materials with different grain size sintered under load. Acta Mater. 52, 1847-1858.

3. Fang, Z., Maheshwari, P., Wang, X., Sohn H.Y., Griffo, A., Riley, R., 2005. An experimental study of the sintering of nanocrystalline WC-Co powders. Int. J. Refract. Met. Hard Mater. 23, 249-257.

4. Lee, G.-H., Kang, S., 2006. Sintering of nano-sized WC-Co powders produced by a gas reduction-carburization process. J. Alloys Compd. 419, 281-289.

5. Wahlberg, S., Grenthe, I., Muhammed, M., 1997. Nanostructured hard material composites by molecular engineering 1. Synthesis from soluble tungstate salts. Nanostruct. Mater. 9, 105-108.

6. Zhu, Y.T., Manthiram, A., 1996. Influence of processing parameters on the formation of WC-Co nanocomposite powder using a polymer as carbon source. Composites Part B. 27, 407-413.

7. Fu, L., Cao, L.H., Fan, Y.S., 2001. Two-step synthesis of nanostructured tungsten carbide-cobalt powders. Scripta Mater. 44, 1061-1068.

8. Nersisyan, H.H., Won, H.I., Won, C.W., Lee, J.H., 2005. Study of the combustion synthesis process of nanostructured WC and WC-Co. Mater. Chem. Phys. 94, 153-158.

9. Wu, X.Y., Zhang, W., Wang, W., Yang, F., Min, J.Y., Wang, B.Q., Guo, J.D., 2004. Ultrafine WC-10Co cemented carbides fabricated by electric-discharge compaction. J. Mater. Res. 19, 2240-2244.

10. Zawrah, M.F., 2007. Synthesis and characterization of WC-Co nanocomposites by novel chemical method. Ceram. Int., 33, 155-161.

11. Shi, X.L., Shao, G.Q., Duan, X.L., Xiong, Z., Yang, H., 2006. Characterizations of WC-10Co nanocomposite powders and subsequently sinterhip sintered cemented carbide. Mater. Charact. 57, 358-370.

12. McCandlish, L.E., Kear, B.H., Kim, B.K., 1992. Processing and properties of nanostructured WC-Co. Nanostruct. Mater. 1, 119-124.

13. Ban, Z.-G., Shaw, L.L., 2002. Synthesis and processing of nanostructured WC-Co materials. J. Mater. Sci. 37, 3397-3403.

14. Hasanpour, A., Mozaffari, M., Amighian, J., 2007. Preparation of Bi-Fe_3O_4 nanocomposite through reduction of Bi_2O_3 with Fe via high-energy ball milling. Physica B. 387, 298-301.

15. Liu, S., Huang, Z.-L., Liu, G., Yang, G.-B., 2006. Preparing nano-crystalline rare earth doped WC/Co powder by high energy ball milling. Int. J. Refract. Met. Hard Mater. 24, 461-464.

16. Mi, S., Courtney, T.H., 1997. Synthesis of WC and WC-Co cermets by mechanical alloying and subsequent hot isostatic pressing. Scripta Mater. 38, 171-176.

17. Chang, W., Skandan, G., Hahn, H., Danforth, S.C., Kear, B.H., 1994. Chemical vapor condensation of nanostructured ceramic powders. Nanostruct. Mater. 4, 345-351.

18. Sohn, H.Y., PalDey, S., 1998. Synthesis of Ultrafine Particles of Intermetallic Compounds by the Vapor-Phase Magnesium Reduction of Chloride Mixtures: Parts I and II. Metall. Mater. Trans. B. 29B, 457-469.

19. Sohn, H.Y., PalDey, S., 1998. Synthesis of Ultrafine Nickel Aluminide Particles by the Hydrogen Reduction of Vapor-Phase Mixtures of $NiCl_2$ and $AlCl_3$. J. Mater. Res. 13, 3060-3069.

20. Sohn, H.Y., PalDey, S., 1998. Synthesis of Ultrafine Particles and Thin Films of Ni_4Mo by the Vapor-Phase Hydrogen Coreduction of the Constituent Metal Chlorides. Mater. Sci. Eng. A. 247, 165-172.

21. Ryu, T., Sohn, H.Y., Han, G., Kim, Y.-U., Hwang, K.S., Mena, M., Fang, Z.Z., 2007. Nanograined WC-Co composite powder by chemical vapor synthesis," Metall. Mater. Trans. B. 39B, 1-6.

22. Won, C.-W., Chun, B.-S., Sohn, H.Y., 1993. Preparation of ultrafine tungsten carbide powder by CVD method from WCl_6-C_2H_2-H_2 mixtures. J. Mater. Res. 8, 2702-2708.

23. Fitzsimmons, M., Sarin, V.K., 1995. Comparison of WCl_6-CH_4-H_2 and WF_6-CH_4-H_2 systems for growth of WC coatings. Surf. Coat. Technol. 76, 250-255.

24. Kim, J.C., Kim, B.K., 2004. Synthesis of nanosized tungsten carbide powder by the chemical vapor condensation process. Scripta Mater. 50, 969-972.

25. Gao, L., Kear, B.H., 1995. Low temperature carburization of high surface area tungsten powders. Nanostruct. Mater. 5, 555-569.

26. Fluent 6.3.26, User's Guide. Fluent Inc., Lebanon, NH, 2003.

27. FLUENT 6 Population Balance Model Manual. Fluent Inc., Lebanon, NH, 2004.

28. Kodas, T., Hampden-Smith, M., 1999. Aerosol Processing of Materials, John Wiley & Sons Inc, New York, pp. 89.

29. Bolsaitis, P.P., McCarthy, J.F., Mohiuddin, G., 1987. Formation of Metal Oxide Aerosols for Conditions of High Supersaturation. Aerosol Sci. Technol. 6, 225-246.

30. Ji, Y., Sohn, H.Y., Jang, H.D., Wan, B., Ring, T.A., 2007. Computational Fluid Dynamic Modeling of a Flame Reaction Process for Silica Nanopowder Synthesis from Tetraethylorthosilicate. J. Am. Ceram. Soc., 90, 3838-3845.

31. Hojo, J., Oku, T., Kato, A., 1978. Tungsten carbide powders produced by the vapor phase reaction of the WCl_6-CH_4-H_2 system. J. Less-Common Met. 59, 85-95.

32. Olivas-Martinez, M., Sohn, H.Y., Jang, H.D.,2008. Silica nanopowder from waste silicon sludge and CFD modeling of the flame spray pyrolysis process. Rewas 2008, Global Symposium on Recycling, The Minerals, Metals & Materials Society, 3, 631-638.

Table 1. Nucleation rate and growth rate constants with average particle size and unreacted WCl_6 concentration.

Experimental conditions: WCl_6 (0.04 g/min), CH_4 (0.1 L/min at 25°C and 86.1 kPa), H_2 (0.25 L/min at 25°C and 86.1 kPa), Ar (0.75 L/min at 25°C and 86.1 kPa), and reaction temperature (1400°C) Measured average particle size based on specific surface area: 22.2 nm WCl_6 is completely consumed in the reaction					
k_n ($m^3 \cdot kmol^{-1} \cdot s^{-1}$)	k_g ($m^7 \cdot kmol^{-2} \cdot s^{-1}$)	Ave. particle size based on specific surface area (nm)	c.v.	% remaining unreacted WCl_6 at outlet	Comments on computation
1×10^{-5}	1×10^{-1}	12.2	0.33	98	converged
	1.8×10^{-1}	21.4	0.33	90	converged
	1	64.5	0.37	33	converged
1×10^{-4}	1×10^{-1}	11.6	0.33	85	converged
	2.4×10^{-1}	21.2	0.35	50	converged
	1	44.3	0.41	22	converged
1×10^{-3}	1×10^{-1}	9.2	0.35	54	converged
	5.4×10^{-1}	22.3	0.42	20	converged
	1	30.3	0.47	10	converged
$1.\times10^{-2}$	1×10^{-1}	6.5	0.37	33	converged
	1.5	21.9	0.56	1.2×10^{-3}	converged
	10	39.6	0.66	2.4×10^{-14}	converged
1×10^{-1}	1×10^{-1}	4.3	0.41	22	converged
	7.5	**21.7**	**0.67**	**1×10^{-19}**	converged
	10	23.9	0.67	1×10^{-23}	unstable, residuals do not approach asymptotic value
1	30	-	-	-	divergence detected
10	1.5×10^{2}	-	-	-	not converged

Figure captions

Figure 1. Reactor wall temperature profile and geometry.

Figure 2. Contour of temperature (K) inside the reactor.

Figure 3. Contour of velocity magnitude (m/s).

Figure 4. Contour of mole fraction of WCl_6.

Figure 5. Contour of mole fraction of H_2.

Figure 6. Contour of mole fraction of CH_4.

Figure 7. Contour of nucleation rate of WC particles (#/m^3 s).

Figure 8. Contour of growth rate of WC particles (m/s).

Figure 9. Contour of WC particle size (nm).

Figure 10. Arrhenius plot of the calculated apparent activation energy of the growth rate.

Figure 1

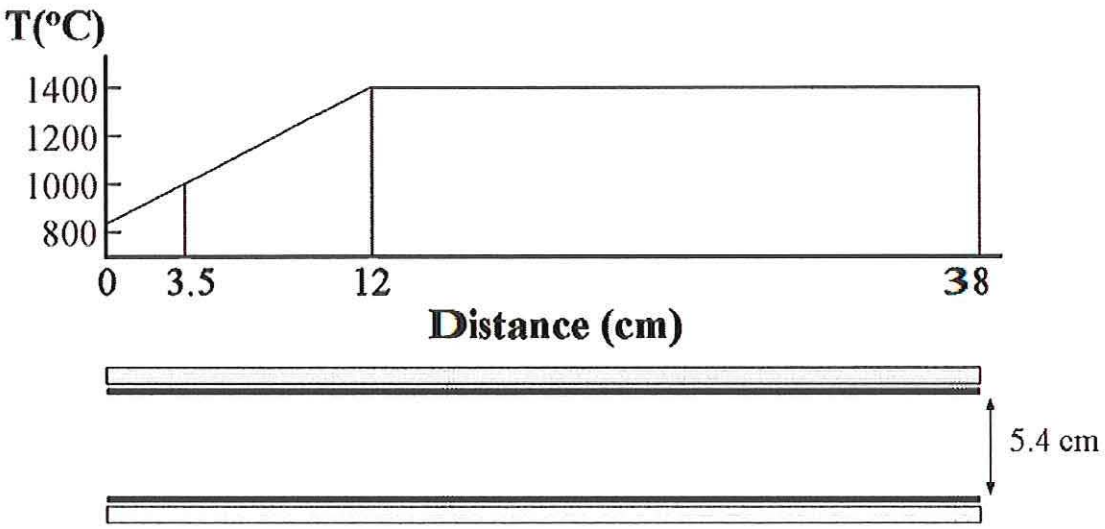

Figure 2

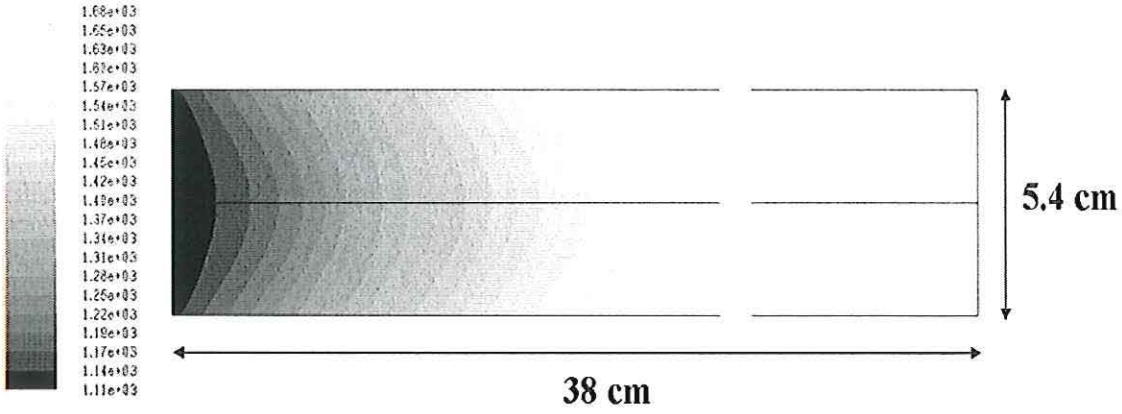
1.68e+03
1.65e+03
1.63e+03
1.60e+03
1.57e+03
1.54e+03
1.51e+03
1.48e+03
1.45e+03
1.42e+03
1.40e+03
1.37e+03
1.34e+03
1.31e+03
1.28e+03
1.25e+03
1.22e+03
1.19e+03
1.17e+03
1.14e+03
1.11e+03
5.4 cm
38 cm

Figure 3

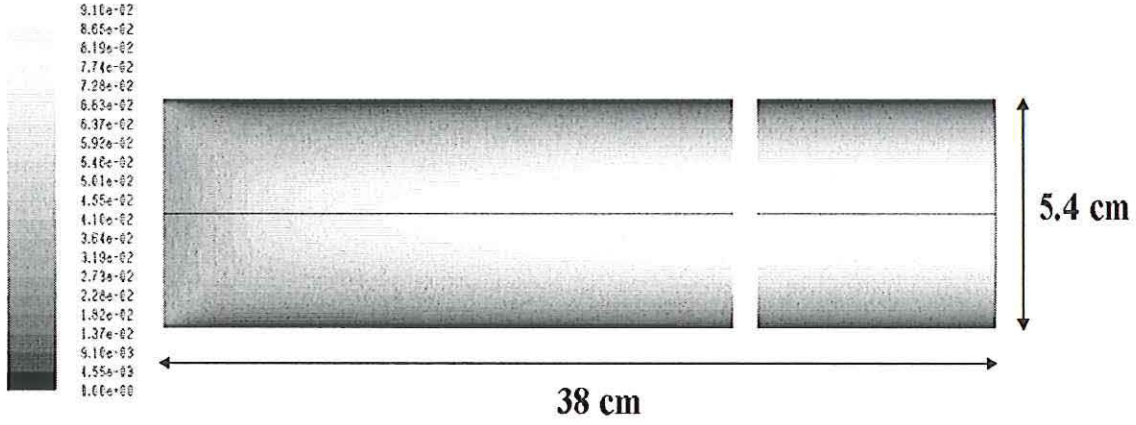
9.10e-02
8.65e-02
8.19e-02
7.74e-02
7.28e-02
6.83e-02
6.37e-02
5.92e-02
5.46e-02
5.01e-02
4.55e-02
4.10e-02
3.64e-02
3.19e-02
2.73e-02
2.28e-02
1.82e-02
1.37e-02
9.10e-03
4.55e-03
0.00e+00
5.4 cm
38 cm

Figure 4

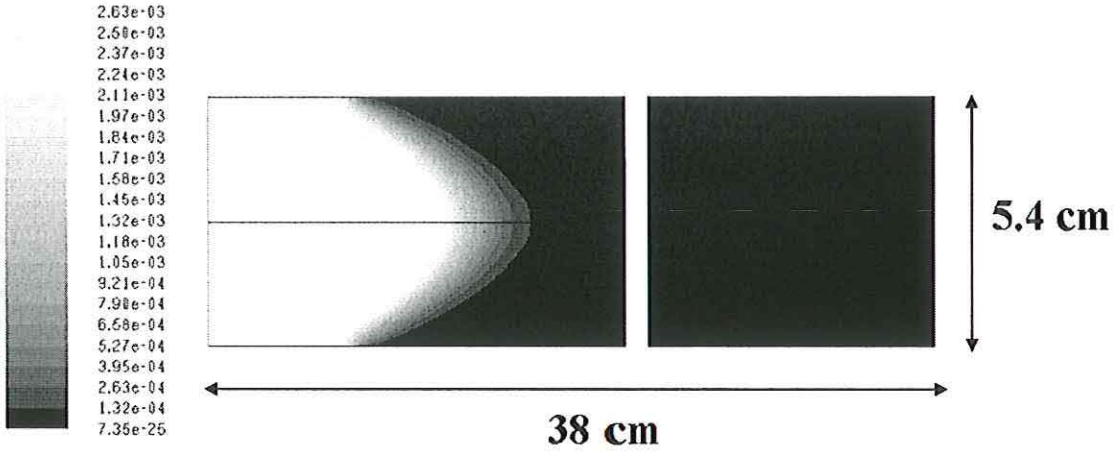
2.63e-03
2.50e-03
2.37e-03
2.24e-03
2.11e-03
1.97e-03
1.84e-03
1.71e-03
1.58e-03
1.45e-03
1.32e-03
1.18e-03
1.05e-03
9.21e-04
7.90e-04
6.58e-04
5.27e-04
3.95e-04
2.63e-04
1.32e-04
7.35e-25
5.4 cm
38 cm

Figure 5

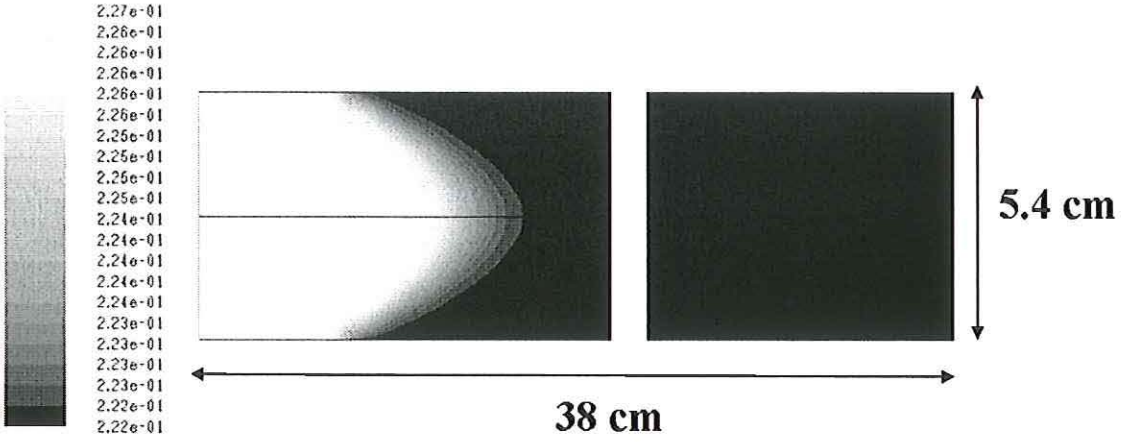
2.27e-01
2.26e-01
2.26e-01
2.26e-01
2.26e-01
2.26e-01
2.25e-01
2.25e-01
2.25e-01
2.25e-01
2.24e-01
2.24e-01
2.24e-01
2.24e-01
2.24e-01
2.23e-01
2.23e-01
2.23e-01
2.23e-01
2.22e-01
2.22e-01
5.4 cm
38 cm

Figure 6

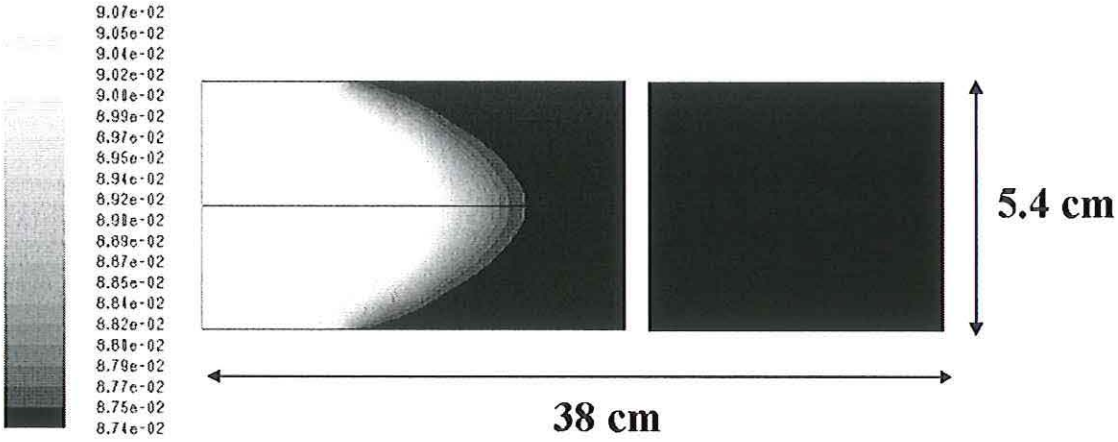
9.07e-02
9.05e-02
9.04e-02
9.02e-02
9.01e-02
8.99e-02
8.97e-02
8.95e-02
8.94e-02
8.92e-02
8.91e-02
8.89e-02
8.87e-02
8.85e-02
8.84e-02
8.82e-02
8.81e-02
8.79e-02
8.77e-02
8.75e-02
8.74e-02
5.4 cm
38 cm

Figure 7

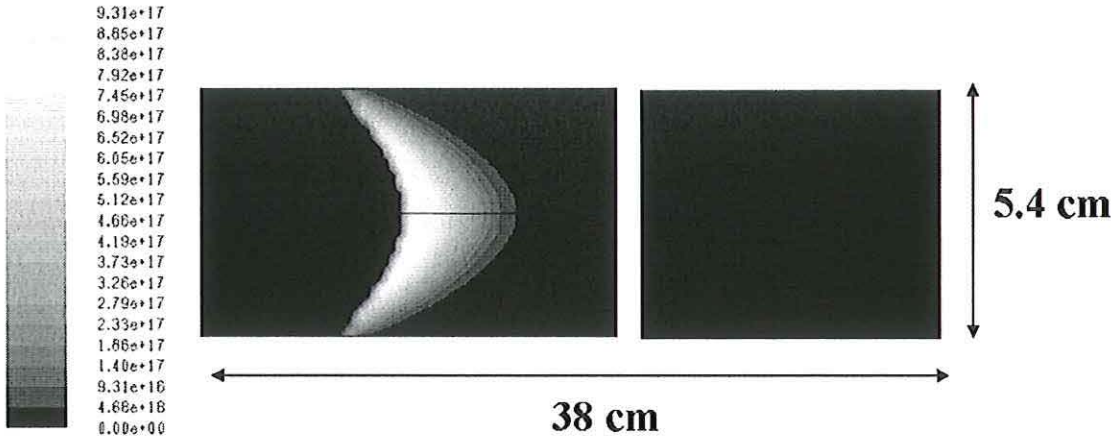
9.31e+17
8.85e+17
8.38e+17
7.92e+17
7.45e+17
6.98e+17
6.52e+17
6.05e+17
5.59e+17
5.12e+17
4.66e+17
4.19e+17
3.73e+17
3.26e+17
2.79e+17
2.33e+17
1.86e+17
1.40e+17
9.31e+16
4.66e+16
0.00e+00
5.4 cm
38 cm

Figure 8

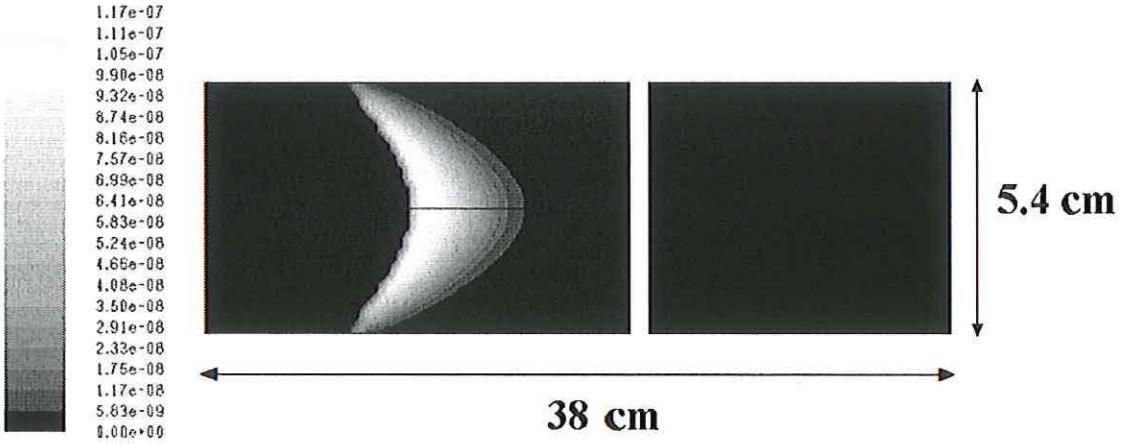
1.17e-07
1.11e-07
1.05e-07
9.90e-08
9.32e-08
8.74e-08
8.16e-08
7.57e-08
6.99e-08
6.41e-08
5.83e-08
5.24e-08
4.66e-08
4.08e-08
3.50e-08
2.91e-08
2.33e-08
1.75e-08
1.17e-08
5.83e-09
0.00e+00
5.4 cm
38 cm

Figure 9

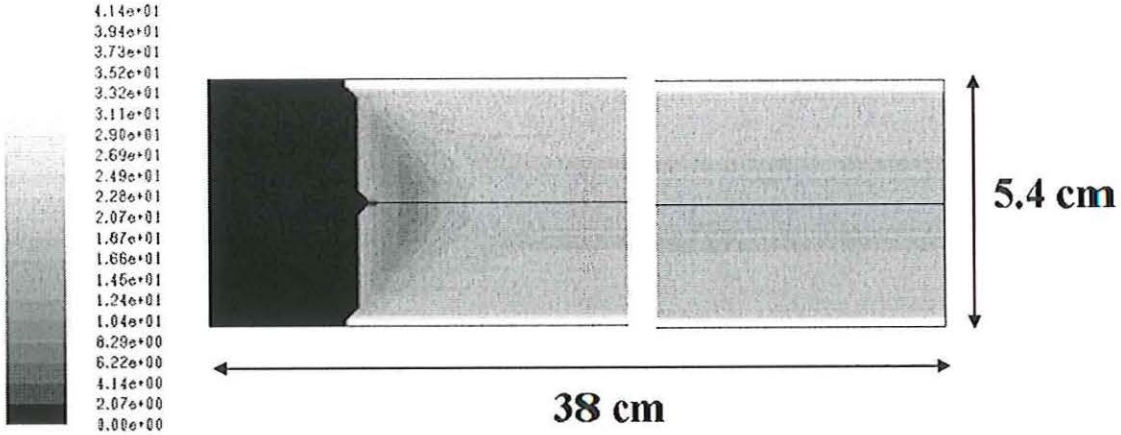
4.14e+01
3.94e+01
3.73e+01
3.52e+01
3.32e+01
3.11e+01
2.90e+01
2.69e+01
2.49e+01
2.28e+01
2.07e+01
1.87e+01
1.66e+01
1.45e+01
1.24e+01
1.04e+01
8.29e+00
6.22e+00
4.14e+00
2.07e+00
0.00e+00
5.4 cm
38 cm

Figure 10

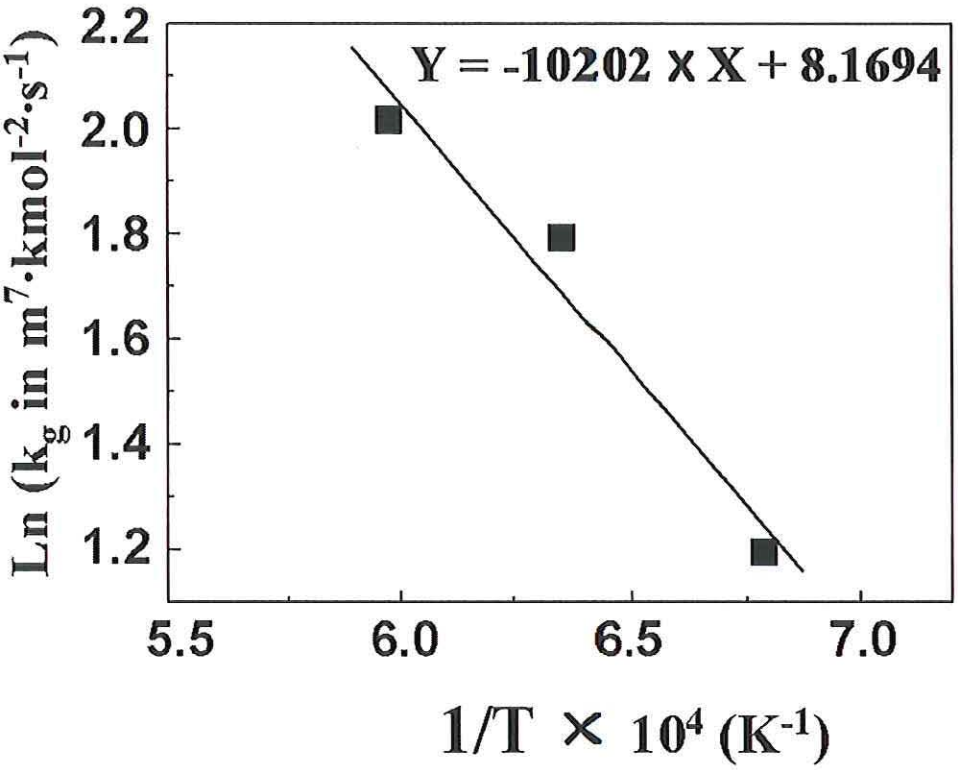
Y = -10202 X X + 8.1694
Ln (k_g in $m^7 \cdot kmol^{-2} \cdot s^{-1}$)
2.2
2.0
1.8
1.6
1.4
1.2
5.5
6.0
6.5
7.0
1/T × 10^4 (K^{-1})